nature portfolio

https://doi.org/10.1038/s41567-021-01336-7

Supplementary information

Surface-tension-induced budding drives alveologenesis in human mammary gland organoids

Appendix A: Supplementary Experimental Results

1. Movies

Supp. Movie 1 Cylindrical branches flow into the organoid body after hydrolysis of the collagen matrix.

Supp. Movie 2 Laser ablation of organoids for branches grown in the attached (left) and floating configuration (right).

Supp. Movie 3 Laser ablation in presence of Cytochalasin D.

Supp. Movie 4 Representative examples of cell dynamics over one day. All organoids stem from the same donor (M25) and were grown in floating gels. Notice that branch shape correlates strongly with the type of motion: axial translation in cylindrical branches, rotation in nascent and mature alveoli.

Supp. Movie 5 Long time observation of cell dynamics shows that alveologenesis and collective cell rotation are correlated (donor: M28).

Supp. Movie 6 Addition of HECD1 antibody against E–cadherin abolishes alveolar rotation within 15–25 hours (donor: M25).

Supp. Movie 7 Cell dynamics at 25X magnification. This experiment corresponds to Supplementary Fig. 4a (donor: M25).

Supp. Movie 8 Cell dynamics at 25X magnification. This experiment corresponds to Supplementary Fig. 4b (donor: M25).

2. Donors

Donor	Age (years)	Parity	Alveoli (%)	n
M20	67	2	30	80
M25	22	0	69	133
M26	34	2	60	78
M28	38	1	57	106

Table I. Age, parity, and frequency of alveoli occurrence at days 11-13 and number of branches analysed.

3. Collagen "cage"

Confocal microscopy of organoids grown in fluorescent collagen shows that organoid branches are surrounded by a thin, dense shell of collagen, which results from an irreversible compaction of the bulk collagen matrix due to active cell contractility. This "collagen cage" is thinner at the organoid branch tips and approaches a thickness of up to $h = 10\,\mu\text{m}$ towards the organoid body [1].

To determine whether the cage is also present around spherical alveoli, organoids were cultivated for two weeks in floating gels of collagen I conjugated with Atto 488. Confocal imaging of both cylindrical branches and spherical alveoli was done using a Leica SP8 confocal microscope and a 40X/1.1 water immersion objective. Subsequently, we measured the fluorescence intensity of the collagen network close to the tip of the branches and normalized on the maximum background. We found indeed a layer of strong fluorescence around spherical alveoli [Supplementary Fig. 1]. This suggests that the formation of the alveolus displaces the preexisting collagen cage, inducing a plastic strain of the surrounding ECM as the organoid surface pushes against it. As a corollary, a proteolytic mechanism for alveologenesis - one that would require the dissolution of the fluorescent collagen - seems unlikely.

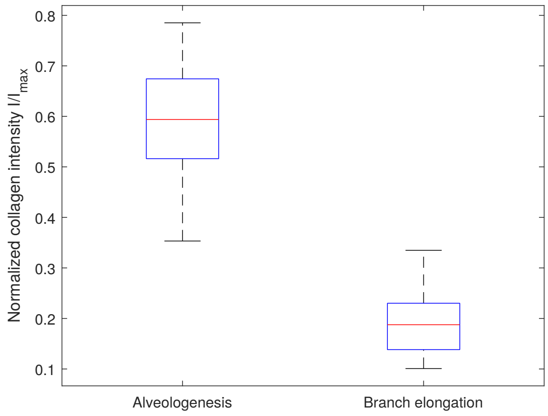

Supplementary Fig. 1. Intensity of the fluorescent collagen cage surrounding spherical alveoli ($n = 15$) and elongating cylindrical branches ($n = 12$)

4. Organoid ablation in the presence of Cytochalasin D

Laser ablation of organoid branches induces a fast recoil of the organoid tissue surrounding the cut. To confirm that this response is due to forces generated by the actomyosin system, we performed experiments in presence of Cytochalasin D (CD), which is known to disrupt actin organization [2]. We incubated organoids with CD at a concentration of 4 µM for 30 min, stained membranes with CellMask for 10 min, and replenished medium containing CD to perform ablation experiments. We found that the recoil response was no longer axially biased and the average strain was significantly lower in the presence of CD (Supplementary Fig. 2). This corroborates that the laser ablation experiments probe cortical tension and that the anisotropy of the response requires an intact actin cytoskeleton.

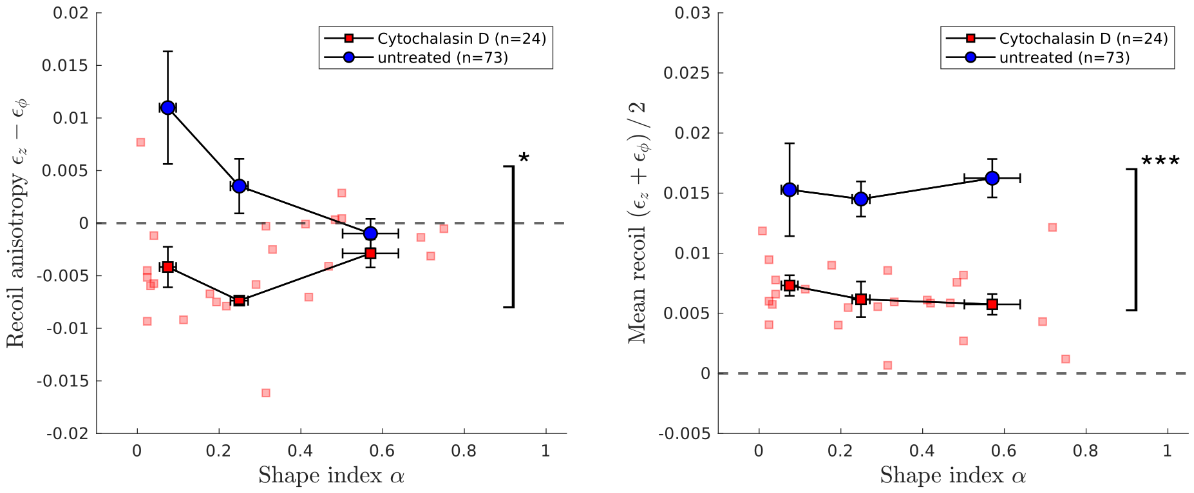

Supplementary Fig. 2. Recoil anisotropy $\epsilon_z - \epsilon_\phi$ and mean recoil $(\epsilon_z + \epsilon_\phi)/2$ as a function of index shape α in presence of Cytochalasin D (red squares). All organoids were grown in floating gels; control points are a replotting of the data shown in Fig. 2c,d (blue circles).

5. Cell boundary segmentation

Stained cell membranes were analysed with the Multicut segmentation tool included in the Ilastik software [3], which decomposes the image into closed regions without dangling edges. The respective boundaries of the cells were traced with a custom Python script. To characterize whether there is an orientational order in the cell population (i.e. a nematic order), we discretized the (smooth) cell boundaries into straight subsegments and computed the histogram of subsegment angles relative to the branch axis angle θ_0. We found that cell boundaries in attached gels are highly biased towards the branch axis, and become increasingly isotropic as the shape index increases (Supplementary Fig. 3). Branches with $\alpha = 0.3$ are already very close to an isotropic distribution of cell boundaries.

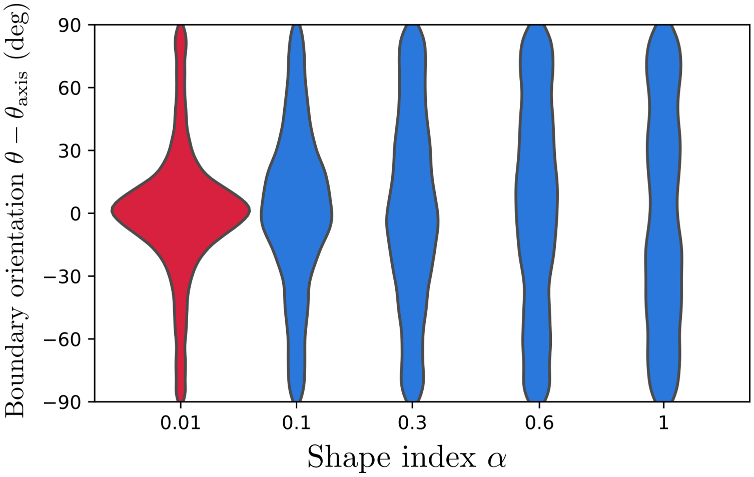

Supplementary Fig. 3. Distribution of cell boundary angles θ relative to the branch axis θ_0 (n=42 organoids) as a function of shape index α for attached (red) and floating gels (blue).

6. Force inference

From the segmented images we sought to estimate the surface tension tensor $\boldsymbol{\tau}$. To that end, we first computed the line tensions acting along individual cell boundaries using the method of force inference developed by Wayne Brodland et al. [4]. This elegant approach assumes a 2D vectorial force balance at every junction of boundaries, providing two scalar equations per junction for a number of unknown line tensions equal to that of boundaries. Arrangements of cells with high connectivity then give an overdetermined homogeneous system of equations. To avoid the trivial zero solution, the equation system is made heterogeneuos by adding an equation that imposes a mean line tension equal to 1. The full system is solved by linear least squares. In this way, we obtained (relative) line tensions γ_i for each cell boundary.

To obtain the surface tension tensor, we must integrate the contributions from each boundary. Specifically, the mean stress tensor in a body can be obtained from the forces acting along its boundary as follows [5]:

$$\bar{\boldsymbol{\tau}} = \frac{1}{2A} \oint dl \Big[\mathbf{f} \otimes \mathbf{x} + \big(\mathbf{f} \otimes \mathbf{x} \big)^T \Big] \,, \tag{A1}$$

where $\mathbf{x}$ refers to the position vectors of each boundary point that is subject a force $\mathbf{f}\, dl$, and A refers to the area of the body. Here, we used a computational scheme that, in the end, reproduced an expression that is analogous to Eq. (A1). First, we divided each boundary into subsegments of constant length $l = 1\,\mu\text{m}$, where segment j of boundary i is oriented in the direction θ_{ij} relative to the tube axis θ_0. Then, we summed the line tensions of all subsegments that point along a given angle θ to obtain the total force distribution $F(\theta) = \sum_{\theta_{ij}=\theta} \gamma_i$. The corresponding force vector is given by $F(\theta)\, \hat{\mathbf{e}}_\theta$, where $\hat{\mathbf{e}}_\theta = (\cos(\theta - \theta_0), \sin(\theta - \theta_0))$ refers to the *unit* vector corresponding to the angle relative to the tube axis, $\theta - \theta_0$. Then, the average tension tensor is proportional to

$$\boldsymbol{\tau} \propto \oint d\theta\, F(\theta)\, \hat{\mathbf{e}}_\theta \otimes \hat{\mathbf{e}}_\theta \,. \tag{A2}$$

Since the line tension is assumed to be constant along each boundary, the total force distribution is symmetric with respect to $\theta \to \theta + \pi/2$. Thus, we calculated the *normalized* axial stress component as follows:

$$\tau_z = \int_{\theta_0 - \pi/2}^{\theta_0 + \pi/2} d\theta\, F(\theta) \cos^2(\theta - \theta_0) \Big/ \int_{\theta_0 - \pi/2}^{\theta_0 + \pi/2} d\theta\, F(\theta)/2 \,, \tag{A3}$$

where the normalization factor ensures that the stress is adimensional and equal to 1 for a uniform stress distribution. Our choice of normalization is justified by the observation that the mean recoil $(\epsilon_z + \epsilon_\phi)/2$ in our laser ablation experiments remained approximately constant for all organoid shapes, cf. Supplementary Fig. 2. A similar equation holds for the circumferential tension:

$$\tau_\phi = \int_{\theta_0-\pi/2}^{\theta_0+\pi/2} d\theta\, F(\theta) \sin^2(\theta-\theta_0) \Bigg/ \int_{\theta_0-\pi/2}^{\theta_0+\pi/2} d\theta\, F(\theta)/2\,. \tag{A4}$$

7. Nuclear anisotropy parameter: an alternative measurement of cellular tension

The shapes of nuclei closely follow the surrounding cell boundaries. We found that nuclei shape could be used to obtain an approximate estimate of the tension anisotropy $\tau_z - \tau_\phi$ determined by force inference, while offering the advantages of less phototoxicity and allowing for precise observation of cell movement. A similar approach was recently discussed and validated by Kong *et al* [6]. Following branch dynamics over 10–20 hours, we found that the nuclear anisotropy parameter χ is large and constant in stable cylindrical branches [Supplementary Fig. 4a]. It robustly decreases shortly before an alveologenic increase in shape index (main text, Fig. 3f), but it can also be seen to increase prior to a reversal of alveologenesis, as the branch resumes longitudinal motion towards the organoid body (Fig. 4b, $t = 10\,\mathrm{h}$).

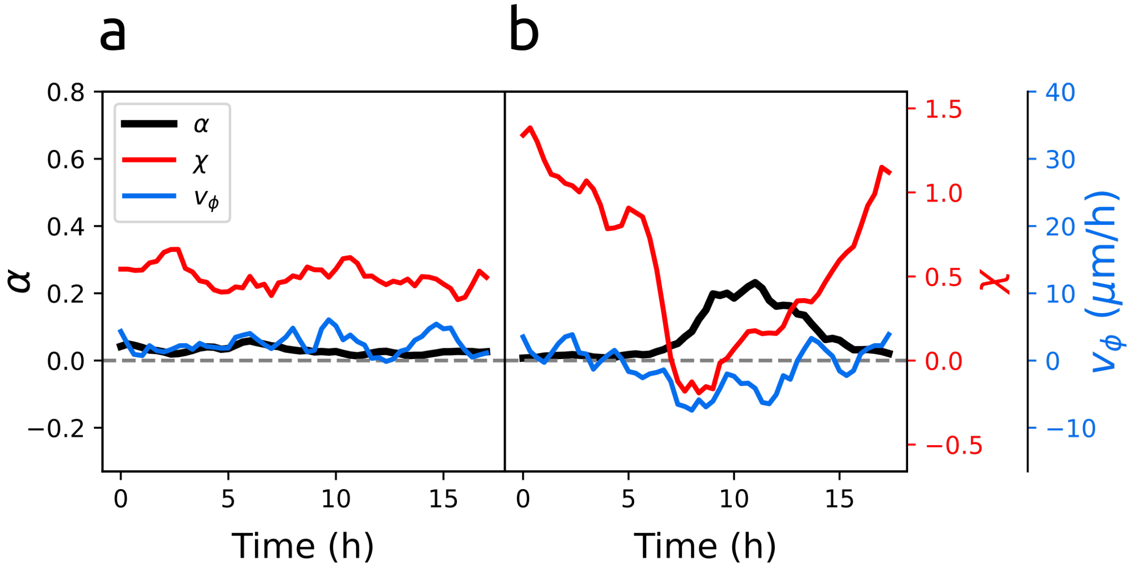

Supplementary Fig. 4. Shape index α, rotation velocity v_ϕ and nuclear anisotropy parameter χ as a function of time for two different experiments. **a,** Data corresponding to Supplementary Movie 7. **b,** Data corresponding to Supplementary Movie 8.

Plotting the replica-averaged nuclear anisotropy parameter as a function of the shape index, we could compare dynamic data with the results of (static) laser ablation and force inference experiments [Supplementary Fig. 5]. We found a good agreement between all datasets, suggesting that the contrasting morphologies of organoids grown in attached and floating gels can be understood in terms of the same underlying physics.

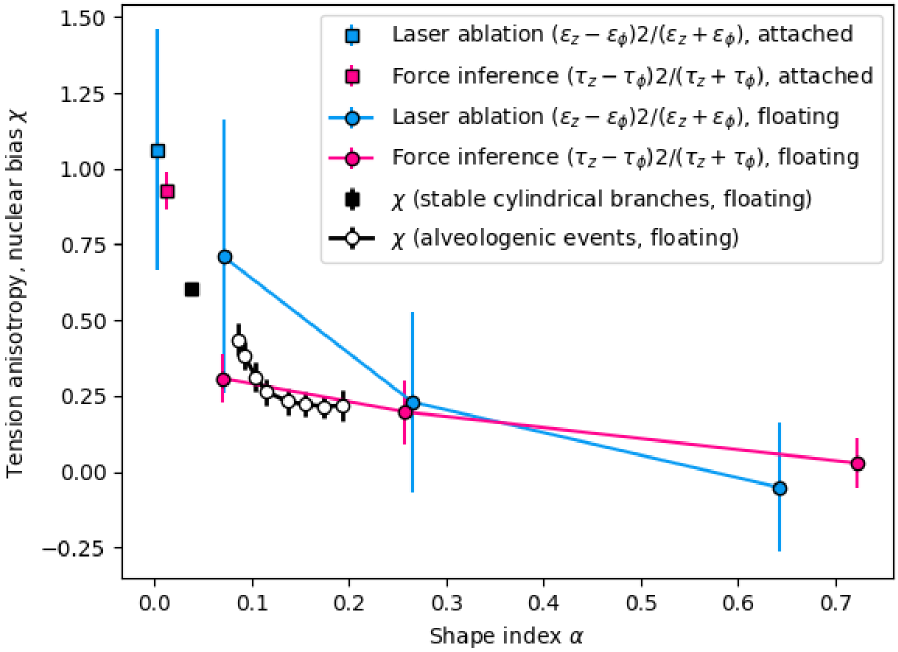

Supplementary Fig. 5. Comparison between laser ablation, force inference and nuclear anisotropy (dynamic) data. Laser ablation and force inference data are replotted from Figs. 2d,h; Nuclear anisotropy data from Fig. 3f.

8. Rotation of alveoli for several donors

The rotational motion of mammary gland organoid branches is largely determined by the branch shape, and the shape index α suffices to characterize this dependency. Branches undergoing translational motion have indexes below 0.3, whereas branches displaying persistent rotation for at least 5 hours have indexes above 0.2 [Supplementary Fig. 6].

To determine the generality of alveolar rotation, we counted the number of branches that showed a sustained rotation around their axis for at least 5 h. For the 4 donors under study, we found that 70%-80% of branches with $\alpha > 0.3$ rotated, whereas most cylindrical branches moved longitudinally (Supplementary Fig. 7).

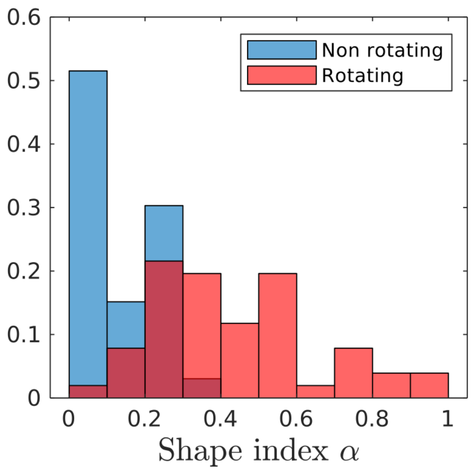

Supplementary Fig. 6. Histogram of shape index α for branches classified as either translating or rotating according to the dominant cell movement mode for 5 hours. Donor: M26.

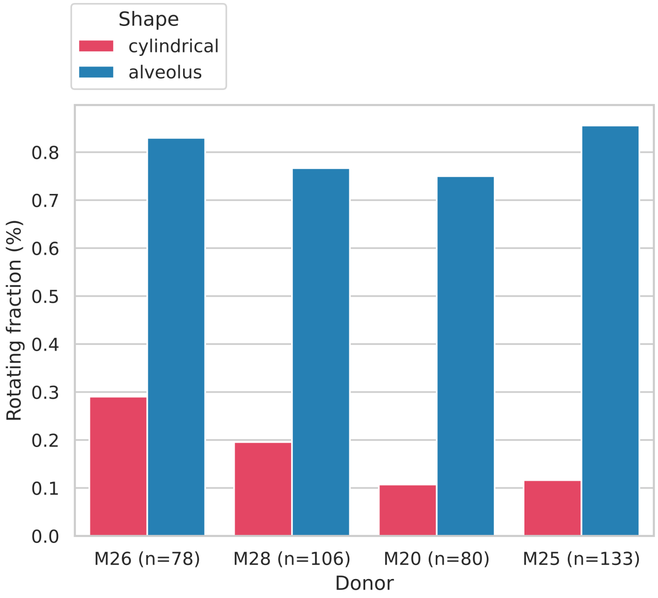

Supplementary Fig. 7. Frequency of rotation in cylindrical branches ($\alpha \leq 0.3$, red) and alveoli ($\alpha \geq 0.3$, blue) for all donors studied (see Supplementary Table 1 for branch sample size).

Appendix B: Supplementary Theoretical Discussion

In the following, we present and discuss in detail our mechanical model of organoid branches. We consider an organoid branch as a shell-like cylindrical tissue, where cell contractility confers an anisotropic surface tension. The lumen of the organoid branch is filled by a viscous fluid, while on the outside it is enveloped by an elastic collagen cage as well as an elastic extracellular matrix. Our theoretical analysis shows that the initial cylindrical shape of an organoid branch becomes unstable against long-wavelength perturbation modes when the circumferential component of the anisotropic surface tension exceeds a critical value. This critical circumferential tension is determined by the elastic properties of the collagen cage and the extracellular matrix. In contrast to the circumferential tension, the axial tension penalizes short-wavelength modes and thus only affects the wavelength of the fastest-growing mode, but not the onset of the shape instability itself.

After choosing a suitable (i.e. cylindrical) coordinate system, we discuss the mechanical stresses that act on organoid branches: active cell contractility, passive bending of the collagen cage and deformations of the extracellular matrix. Since viscous stresses asymptotically vanish if the dynamics of the organoid branch is sufficiently slow, the applied mechanical stresses determine whether a tubular shape is stable or not. To then find conditions under which a tubular conformation becomes mechanically unstable, we consider linear shape perturbations of a tubular shell that has a homogeneous initial radius and vanishing mechanical stress (mechanical steady state). Then, by expanding our theory beyond this linear regime and considering nonlinear contributions to the mechanical stress, we investigate how an organoid branch responds to an increase in surface tension.

1. Choice of coordinate system

We describe an organoid branch as a thin tubular shell that consist of contractile cells, and use a cylindrical coordinate system (r, z, ϕ), where the z-axis is aligned with the centerline of the tube, r measures the radial distance from the centerline, and ϕ is the azimuthal angle [Supplementary Fig. 8]. For the sake of simplicity, we restrict ourselves to a rotationally symmetric geometry, so that $\partial_\phi Q(z, \phi) \equiv \partial_\phi Q(z) = 0$ for any (scalar, vectorial or tensorial) quantity $Q(z, \phi)$.

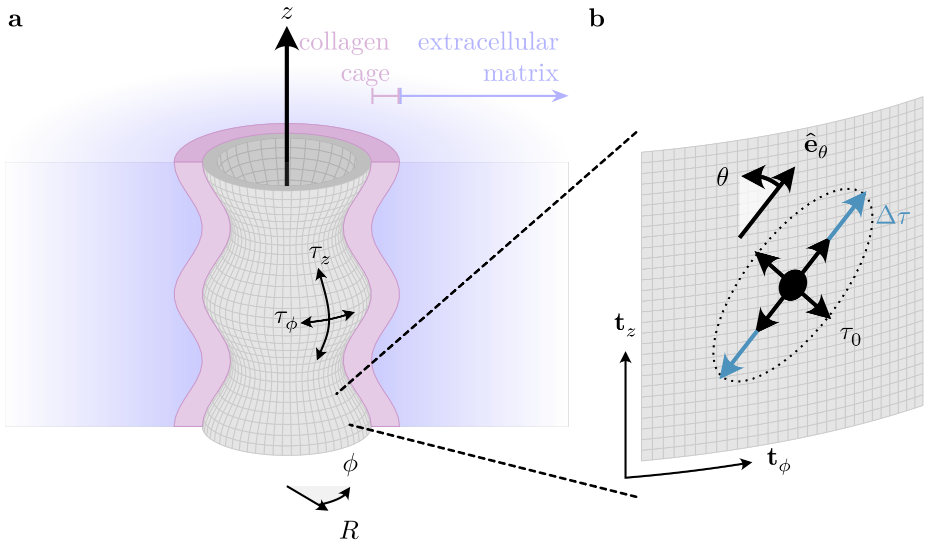

Supplementary Fig. 8. Schematic representation of the organoid branch geometry. **a)** The cell population forms a thin tubular shell (gray), whose lumen is filled by an aqueous solution under hydrostatic pressure p_0. On the outside, the cellular tube is surrounded by a dense and rigid collagen cage (magenta). Further away, the cellular tube is surrounded by a soft extracellular matrix (blue). **b)** Enlarged view of the cell population that forms the surface of the organoid branch. Each cell (within the local tangent plane) is oriented at an angle θ relative to the local axial tangent vector $\mathbf{t}_z$, with corresponding orientation vector $\hat{\mathbf{e}}_\theta$. We consider each cell as a contractile force dipole. To conceptually illustrate how such a contractile force dipole acts, one can envision an idealized cell with diameter d_0 and area A_0 (black circle). The cell cytoskeleton exerts contractile forces on the cell boundary, which we decompose into two contributions: (i) Isotropic contractile forces f_0 correspond to an isotropic tension $\tau_0 \equiv f_0 d_0 / A_0$ (black arrows). (ii) In addition, the contractile cell breaks rotational symmetry in this local frame of reference by increasing contractility ($\Delta f > 0$) or decreasing contractility ($\Delta f < 0$) along its axis $\hat{\mathbf{e}}_\theta$. Therefore, in addition to the isotropic part of cell tension, there is also an anisotropic contribution $\Delta\tau \equiv \Delta f \, d_0 / A_0$.

The tubular shell is located at a distance $r = R(z)$ from the centerline, where it forms an interface between the viscous fluid in the lumen of the organoid branch and the extracellular matrix outside of the organoid. We parameterize this interface by the two coordinates (z, ϕ) and the corresponding position vector field

$$\mathbf{R}(z, \phi) = \begin{bmatrix} R(z)\, \cos\phi \\ R(z)\, \sin\phi \\ z \end{bmatrix} . \tag{B1}$$

The two (orthogonal but non-normalized) tangent vectors that span the surface of the tubular shell are given by

$$\mathbf{t}_z = \begin{bmatrix} \partial_z R(z)\,\cos\phi \\ \partial_z R(z)\,\sin\phi \\ 1 \end{bmatrix}, \quad \text{and} \quad \mathbf{t}_\phi = \begin{bmatrix} -R(z)\,\sin\phi \\ R(z)\,\cos\phi \\ 0 \end{bmatrix}. \tag{B2}$$

In the following, we usually omit the argument of the tube radius, $R(z) \equiv R$, to keep the expressions concise. To measure arc distances on the surface of the tubular shell in terms of the coordinates (z, ϕ), we use the metric tensor $g_{ij} = \mathbf{t}_i \cdot \mathbf{t}_j$ [7]:

$$\mathbf{g} \equiv \begin{bmatrix} g_{\phi\phi} & g_{\phi z} \\ g_{\phi z} & g_{zz} \end{bmatrix} = \begin{bmatrix} R^2 & 0 \\ 0 & 1 + (\partial_z R)^2 \end{bmatrix}. \tag{B3}$$

We complete the local coordinate system that spans the surface of the tubular shell by introducing the (outward pointing) *unit* normal vector, $\hat{\mathbf{n}} = (\mathbf{t}_\phi \times \mathbf{t}_z)/\sqrt{\det \mathbf{g}}$, which lies perpendicular to the surface:

$$\hat{\mathbf{n}} = \frac{1}{[1 + (\partial_z R)^2]^{\frac{1}{2}}} \begin{bmatrix} \cos\phi \\ \sin\phi \\ -\partial_z R \end{bmatrix}. \tag{B4}$$

Thus, to summarize, we have defined a local coordinate system on the surface of the tubular shell, which is parameterized by the coordinates (z, ϕ) and spanned by the two tangent vectors $(\mathbf{t}_z, \mathbf{t}_\phi)$ as well as the normal vector $\hat{\mathbf{n}}$.

Next, we determine the shape tensor, $h_{ij} = \hat{\mathbf{n}} \cdot \partial_i \mathbf{t}_j$, which describes the geometrical shape of the tubular shell [7]. Specifically, one can directly read off the two principal curvatures of the tubular shell from the following expression:

$$\mathbf{h} \cdot \mathbf{g}^{-1} = \begin{bmatrix} -\frac{R^{-1}}{[1+(\partial_z R)^2]^{\frac{1}{2}}} & 0 \\ 0 & \frac{\partial_z^2 R}{[1+(\partial_z R)^2]^{\frac{3}{2}}} \end{bmatrix} \equiv \begin{bmatrix} \kappa_\phi & 0 \\ 0 & \kappa_z \end{bmatrix}. \tag{B5}$$

As explained above, we view the organoid branch as a rotationally symmetric cylinder that is parameterized by the distance $R(z)$ of its surface from the centerline. In the present work, we always assume that deformation gradients are small, so that $\partial_z R \ll 1$. Then, the two principal curvatures are simply given by

$$\kappa_\phi \approx -\frac{1}{R}\,, \quad \text{and} \quad \kappa_z \approx \partial_z^2 R\,, \tag{B6}$$

which are used in the remainder of the Supplementary Material. In the upcoming sections, we will discuss the physical processes that can dynamically modify these local geometric properties of the organoid branch.

2. Active cell contractility induces anisotropic tension and Laplace pressure

As discussed in section B 1 "Choice of coordinate system", we describe the organoid branch as a thin tubular shell. At the surface of the organoid branch, contractile cells form a thin confluent tissue. Furthermore, this surface defines an interface between the fluid in the lumen of the organoid branch and the extracellular matrix outside of the organoid branch [Supplementary Fig. 8]. Since the cells are the only active component of our system, their activity determines the dynamics of the organoid branch. Specifically, nonequilibrium cell contractility at the surface of the organoid branch confers an *active interfacial stress* in the form of anisotropic surface tension, as we explain in the following.

Link between cell orientation and tension anisotropy. We consider cells as anisotropic force dipoles [8, 9], where the anisotropy stems from the local orientation of the cells and their cytoskeleton[1]. Before we characterize a population of many cells, we first focus on describing a single cell. To that end, we consider the local reference frame (tangent plane) that is spanned by the two (orthogonal but non-normalized) surface tangent vectors $(\mathbf{t}_z, \mathbf{t}_\phi)$ and whose origin coincides with the position of the cell [Fig. 8b]. The cell is oriented at an angle θ relative to the axial surface tangent vector $\mathbf{t}_z$, so that we represent its orientation with the vector

$$\hat{\mathbf{e}}_\theta = \cos(\theta)\frac{\mathbf{t}_\phi}{\|\mathbf{t}_\phi\|} + \sin(\theta)\frac{\mathbf{t}_z}{\|\mathbf{t}_z\|} \equiv \begin{bmatrix}\cos(\theta)\\ \sin(\theta)\end{bmatrix}\,. \tag{B7}$$

Due to orientational order in its cytoskeleton, the cell can exert stronger (or weaker) tensile

---

[1] In section A 6 "Force inference", we have represented the average tension tensor of a cell as a boundary integral of the forces that act on the cell boundary. Here, we consider the body forces that act as a result of intracellular actomyosin contractility. In the co-moving reference frame of a non-deforming cell, both descriptions are equivalent because internal stresses must exactly balance externally applied stresses.

forces along its axis $\hat{\mathbf{e}}_\theta$ than along the perpendicular axis. Therefore, we split the tension of a cell into two contributions: (i) an isotropic *base* tension τ_0 that preserves rotational symmetry in our local reference frame and (ii) an additional anisotropic tension $\Delta\tau$ along the direction specified by the vector $\hat{\mathbf{e}}_\theta$ that breaks rotational symmetry in our local reference frame. Taken together, we model cell contractility with the following cell tension tensor[2]:

$$\boldsymbol{\tau}(\theta) = \tau_0\, I_2 + \Delta\tau\, \hat{\mathbf{e}}_\theta \otimes \hat{\mathbf{e}}_\theta\,. \tag{B8}$$

The diagonal elements of the cell tension tensor then correspond to the axial τ_z and the circumferential tension τ_ϕ, respectively:

$$\boldsymbol{\tau}(\theta) = \begin{bmatrix} \tau_0 + \Delta\tau\cos^2(\theta) & \Delta\tau\cos(\theta)\sin(\theta) \\ \Delta\tau\cos(\theta)\sin(\theta) & \tau_0 + \Delta\tau\sin^2(\theta) \end{bmatrix} \equiv \begin{bmatrix} \tau_z & \ddots \\ \ddots & \tau_\phi \end{bmatrix}. \tag{B9}$$

Now consider a population of cells in which the cells differ in their orientations $\hat{\mathbf{e}}_\theta$ and exert an anisotropic tension $\boldsymbol{\tau}(\theta)$. We statistically represent the occurrence of different cell orientations θ by the probability density function $P(\theta)$, which we refer to as *angular distribution of cell orientations*. The average tension tensor in the confluent tissue is then given by the weighted average $\bar{\boldsymbol{\tau}} = \int_{-\pi}^{\pi} d\theta\, P(\theta)\, \boldsymbol{\tau}(\theta)$. Thus, the off-diagonal terms of the average tension tensor in the confluent tissue vanish for a symmetric angular distribution of cell orientations, $P(\theta) = P(-\theta)$. Furthermore, we note that the trace of the cell tension tensor for each cell is independent of the cell's orientation, $\mathrm{tr}(\boldsymbol{\tau}) = \tau_z + \tau_\phi = 2\tau_0 + \Delta\tau$. Therefore, since the angular distribution of cell orientation is normalized, $\int_{-\pi}^{\pi} d\theta\, P(\theta) = 1$, the trace of the average tension tensor in the confluent tissue is constant,

$$\mathrm{tr}\, \bar{\boldsymbol{\tau}} = \bar{\tau}_z + \bar{\tau}_\phi = 2\tau_0 + \Delta\tau\,. \tag{B10}$$

In other words, the total tension in the confluent tissue, $\bar{\tau}_z + \bar{\tau}_\phi$, is independent of the angular distribution of cell orientations. This explains our experimental finding that the sum of the axial and the circumferential tension remains constant for all experiments.

If all cells are oriented in the same direction, e.g. along the centerline of the organoid branch so that $P(\theta) = \delta(\theta)$, then the difference between the axial and the circumferential

---

[2] One can also rationalize this form by performing a boundary integral of the forces that act on the cell boundary, analogous to section A 6 “Force inference”.

tension is simply given by $\bar{\tau}_z - \bar{\tau}_\phi = \Delta\tau$. In contrast, if all cells are oriented randomly, $P(\theta) = 1/(2\pi)$, then axial and circumferential tension are equal $\bar{\tau}_z = \bar{\tau}_\phi$. Thus, if the cells are initially aligned with the axial surface tangent vector $\mathbf{t}_z$ (i.e. aligned with the centerline of the tube) and subsequently *randomize* their orientation, then the circumferential tension in the tissue will effectively increase at the expense of a decreasing axial tension. These theoretical considerations imply that in our experiments the predominant process underlying tension anisotropy is due to the reorientation of cells and not a change in their tensile properties τ_0 and $\Delta\tau$.

In the present section, we have investigated how the orientation of cells, treated as anisotropic force dipoles, affects the average tension in a confluent tissue. From here on, we will not describe the precise distribution of cell orientation. Instead, we simplify our description by considering only an axial tension τ_z and an independent circumferential tension τ_ϕ on the surface of the tubular shell (i.e. the organoid branch); we also simplify notation by omitting the overline indicating the population average.

Tension anisotropy leads to generalized Laplace pressure. Next, we discuss how *anisotropic* surface tension couples to the organoid shape and how it is different from an isotropic surface tension. We consider cells as active agents that perform work as they deform the organoid branch (i.e. tubular shell). Instead of formally carrying out variational calculus of surfaces, in this section we omit the corresponding surface integrals by considering the dynamics of an (approximately homogeneous) infinitesimal surface patch with area A. In the case of isotropic surface tension τ_{iso}, the cells perform the work $\delta W = -\tau_{iso}\,\delta A$ [10] as they change the area of the surface patch on the tubular shell by δA. For a curved surface such as the organoid branch, one can relate a change in surface area to a displacement of the surface patch by a distance δu along its normal vector[3,4], $\delta A = -(\kappa_\phi + \kappa_z)\,\delta u\, A$ [7]. Thus, any

---

[3] This relation can be easily checked for spherical geometries (with radius R, azimuthal angle ϕ and polar angle ϑ), where a surface patch has area $A \equiv R^2\, d\vartheta\, d\cos\phi$. Then, radial movement of the surface patch by a distance δu changes its area by $\delta A = \partial_R A\,\delta u = 2R\, d\vartheta\, d\cos\phi\,\delta u$. Identifying the curvature of the sphere with $\kappa_\phi = \kappa_\vartheta = -1/R$, one then finds $\delta A = -(\kappa_\phi + \kappa_\vartheta)\,\delta u\, A$. One can perform an analogous calculation for straight tubular geometries.

[4] For general (i.e. undulating) tubular geometries, one has to determine how the surface area changes upon a deformation $\delta u(z)$ via variational calculus. The surface area of the cylinder is given by the functional $A[u] = 2\pi \int dz \sqrt{1 + (\partial_z u)^2}\,(R_0 + u)$. The variation of the surface area of the cylinder is then also a functional: $\delta A[u] = -2\pi \int dz\,(R_0 + u)\,(\kappa_\phi + \kappa_z)\,\delta u(z)$, where the curvatures are given by Eq. (B5). For sufficiently thin patches, one can then approximate their surface area as $2\pi \int dz\,(R_0 + u) \approx 2\pi dz\,(R_0 + u) \equiv A$, to arrive at the expression in the main text.

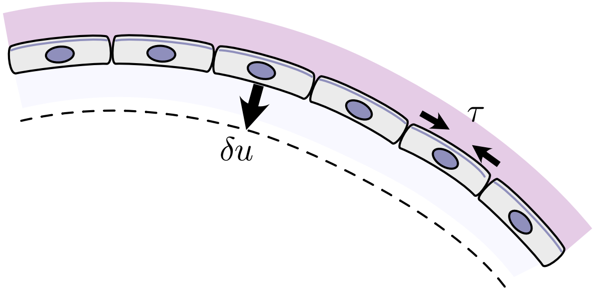

Supplementary Fig. 9. Illustration of a surface that moves by a distance δu, thereby decreasing its surface area from A (initial configuration, sketch) to $A+\delta A$ (dashed line), where $\delta A<0$. The surface consists of contractile cells, which exert a tension τ that drives the dynamics.

surface patch that is curved towards its direction of motion, $(\kappa_\phi+\kappa_z)\,\delta u>0$, will effectively contract [Fig. 9]. This results in a cell-induced Laplace pressure $\Delta p_{iso}=\frac{\delta W}{A\delta u}=(\kappa_\phi+\kappa_z)\,\tau_{iso}$. Note that this is a generalization of the expression for the Laplace pressure in a sphere, $\Delta p_{iso}\sim 2\tau_{iso}/R$, to generic surfaces.

Unlike isotropic tension, *anisotropic* tension breaks rotational symmetry, so that one must individually consider the (relative) length changes that occur in different directions as the cells deform the organoid branch. Here, it helps to envision (anisotropic) surface tension as a meshwork of ropes, which are aligned along the axis and along the circumference of the tubular shell, respectively. Then, one may associate axial tension with the work that is required for increasing the (relative) length of the tubular shell, and circumferential tension with the work that is required for increasing the (relative) circumference of the tubular shell. In summary, one then has:

$$\delta W=-\left(\tau_z\,\frac{\delta\ell_z}{\ell_z}+\tau_\phi\,\frac{\delta\ell_\phi}{\ell_\phi}\right)\,A\,, \tag{B11}$$

where ℓ_z and ℓ_ϕ refer to the arc lengths on the surface and $A=\ell_z\,\ell_\phi$ is the area of the corresponding surface patch. Upon a displacement of the organoid surface by a distance δu along its normal vector, the circumferential arc length ℓ_ϕ and the axial arc length ℓ_z change as follows[5,6]:

$$\begin{aligned} \delta\ell_\phi &= -\kappa_\phi \, \delta u \, \ell_\phi \\ \delta\ell_z &= -\kappa_z \, \delta u \, \ell_z \, . \end{aligned} \tag{B12}$$

With these considerations, the (generalized) Laplace pressure on the tubular shell, $\frac{\delta W}{A \delta u}$, is given by:

$$\Delta p_\tau = \tau_\phi \kappa_\phi + \tau_z \kappa_z \, . \tag{B13}$$

By explicitly inserting the expressions for the axial and the circumferential curvatures, Eq. (B6), we obtain:

$$\Delta p_\tau = -\frac{\tau_\phi}{R} + \tau_z \, \partial_z^2 R \, . \tag{B14}$$

The generalized Laplace pressure, Eq. (B14), must be balanced by stresses in the fluid (specifically, viscous stresses and hydrostatic pressure) as well as by elastic stresses in the extracellular matrix [discussed in sections A 3 "Collagen "cage"" and B 4 "Bulk extracellular matrix elasticity does not significantly affect tube stability"].

3. Collagen cage envelops organoids and confers mechanical stability

In this section, we discuss the elastic properties of the extracellular matrix, which puts constraints on the deformations of the thin tubular shell (i.e. the organoid branch). We base our model on the experimental determination of the density and thickness of the collagen cage that surrounds branches and alveoli, as discussed above (section A 3 "Collagen "cage""). This is built by the contractile activity of the cells in the organoid branches, which gives rise to complex mechanical properties. Furthermore, its mechanical properties currently cannot be separated from the mechanical properties of the surrounding collagen matrix and the mechanical properties of the cells. As a consequence, its elastic modulus is unknown and not readily accessible to experiments. In this section, we estimate the elastic modulus of the collagen cage.

Estimate for the rigidity of the collagen cage. From fluorescence intensity mea-

---

[5] This relation can be illustrated as follows. Any curved line segment can be understood as a circle segment with angle $d\phi$ and radius R. The arc length of this line segment is then given by $\ell_\phi = R \, d\phi$. Upon radial displacement by a distance δu, the arc length changes by $\delta\ell_\phi = \partial_R \ell_\phi \, \delta u = d\phi \, \delta u$. Identifying the curvature as $\kappa_\phi \equiv -1/R$, one then finds $\delta\ell_\phi = -\kappa_\phi \, \delta u \, \ell_\phi$.

[6] Note that from these relations one also finds $\delta A = \ell_z \delta\ell_\phi + \ell_\phi \delta\ell_z = -(\kappa_\phi + \kappa_z) \, \delta u \, A$, where $A \equiv \ell_\phi \ell_z$.

surements, we know that the collagen cage has a roughly 5-fold higher density than the bulk collagen [1]. We now assume that the cage is structurally similar to bulk collagen, but concentrated by a factor of 5. In general, the elastic modulus of collagen increases with the concentration roughly in a power-law manner with an exponent in the range of 2.2–2.6 [11, 12]. At our standard concentration of $\rho_{\text{bulk}} = 1.3\,\text{mg}\,\text{ml}^{-1}$, we measured the shear modulus to be $\mu \simeq 7\,\text{Pa}$ (data not shown; see [12]). The corresponding elastic modulus can be calculated from the shear modulus by using [5] $E = 2\,(1+\nu)\,\mu$, where the Poisson ratio can be approximated as $\nu = 0.5$ [13]. Taking a concentration-dependence exponent of 2.2, we thus obtain a lower estimate of $E_{cage} = 0.72\,\text{kPa}$ for the elastic modulus of the collagen cage. Instead taking a concentration-dependence exponent of 2.6, we obtain an upper estimate of $E_{cage} = 1.38\,\text{kPa}$ for the elastic modulus of the collagen cage.

Passive stretching of the collagen cage induces elastic stresses. As discussed in the previous paragraphs, organoid branches and alveoli are surrounded by a thin, dense "collagen cage", which we model as a thin elastic shell. In the following, we first discuss how much energy is stored in elastic deformations of the collagen cage, which includes bending and stretching [14]. Then, we determine the corresponding elastic boundary stresses that act on the surface of a deformed tubular shell. Since we account for the mechanical properties of cells by treating them as contractile force dipoles, cf. section B 2 "Active cell contractility induces anisotropic tension and Laplace pressure", we assume in the following that the elastic response of the tubular shell is dominated by the elastic properties of the collagen cage and not the cell sheet[7].

We begin by considering stretching (or compression) of the collagen cage. To parameterize the corresponding deformation field $\mathbf{u}(z)$, we use a cylindrical coordinate system that is spanned by the normalized basis vectors [cf. section B 4 "Bulk extracellular matrix elasticity does not significantly affect tube stability"]:

$$\hat{\mathbf{b}}_r = \begin{bmatrix} \cos\phi \\ \sin\phi \\ 0 \end{bmatrix}, \quad \hat{\mathbf{b}}_z = \begin{bmatrix} 0 \\ 0 \\ 1 \end{bmatrix}, \quad \text{and} \quad \hat{\mathbf{b}}_\phi = \begin{bmatrix} \sin\phi \\ \cos\phi \\ 0 \end{bmatrix}. \tag{B15}$$

As we assume that the deformation gradients of the surface are small, $\partial_z R \ll 1$, the radial

---

[7] A more detailed approach would have to differentiate between the mechanical in-plane deformation of the collagen cage and the mechanical in-plane deformation of the cell sheet, because motile cells can move relative to the substrate that they adhere to.

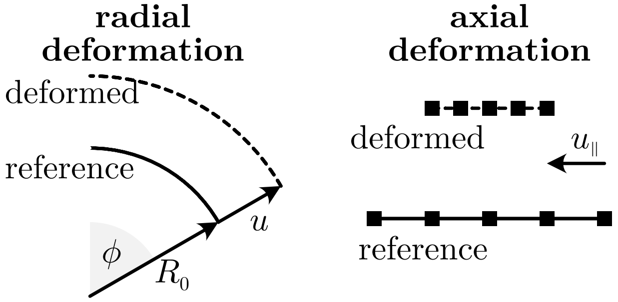

Supplementary Fig. 10. Illustration of radial deformations (left) and axial deformations (right). Any elastic body that is stretched or compressed exhibits elastic stresses that counteract these deformations.

basis vector coincides with the *unit* surface normal, $\hat{\mathbf{b}}_r \approx \hat{\mathbf{n}}$, and the axial basis vector coincides with the (in that case normalized) surface tangent vector, $\hat{\mathbf{b}}_z \approx \hat{\mathbf{t}}_z$, cf. section B 1 “Choice of coordinate system”. We consider $u \equiv u(z)$ as the radial (or *normal*) component of the surface deformation field, which accounts for radial displacements of the surface. Such radial deformations change the radius of the tubular shell from R_0 in its cylindrical reference configuration to $R = R_0 + u$ in its deformed configuration. In addition, we also consider the axial (or *tangential*) component of the surface deformation field, $u_\parallel \equiv u_\parallel(z)$, which however has no effect on the shape of the tubular shell. To summarize, in our cylindrical geometry the surface deformation field is given by $\mathbf{u} = u\,\hat{\mathbf{b}}_r + u_\parallel\,\hat{\mathbf{b}}_z$

In the present work, we analyze the linear stability of the tubular shell and therefore consider only infinitesimal deformations of the collagen cage from its cylindrical reference configuration[8]. The corresponding linearized surface strain tensor is given by [5]:

$$\boldsymbol{\epsilon}_{lin} = \frac{1}{2}\left[\boldsymbol{\nabla} \otimes \mathbf{u} + (\boldsymbol{\nabla} \otimes \mathbf{u})^T\right] = \sum_{i,j\in\{\phi,z\}} \epsilon_{ij}\,\hat{\mathbf{b}}_i \otimes \hat{\mathbf{b}}_j\,, \tag{B16}$$

where the circumferential component $\epsilon_{\phi\phi}$ and the axial component ϵ_{zz} of the surface strain tensor are given by [Fig. 10]:

$$\epsilon_{\phi\phi} \approx \frac{u}{R_0}\,, \quad \text{and} \quad \epsilon_{zz} \approx \partial_z u_\parallel\,. \tag{B17}$$

Circumferential strain $\epsilon_{\phi\phi}$ corresponds to a change of the circumferential arc length ℓ_ϕ due

---

[8] For a nonlinear analysis, one would have to calculate the nonlinear (Green) strain tensor, $\boldsymbol{\epsilon}_g = \boldsymbol{\epsilon}_{lin} + \frac{1}{2}(\boldsymbol{\nabla}\otimes\mathbf{u})^T \cdot (\boldsymbol{\nabla}\otimes\mathbf{u})$, where $\boldsymbol{\epsilon}_{lin}$ refers to the linear part of the strain tensor (B16). Such an analysis was carried out by Hannezo et al. [15].

to an out-of-plane displacement u, cf. Eq. (B12) and Fig. 9. Axial strain corresponds to a compression or dilatation due to in-plane deformations. Neglecting in-plane shear strain $\epsilon_{z\phi}$, stretching of the tubular shell is associated with the following free energy density per surface area [14]:

$$f_s = \frac{E_{cage}\, h}{2\,(1-\nu^2)}\Big[\epsilon_{\phi\phi}^2 + \epsilon_{zz}^2 + 2\nu\epsilon_{\phi\phi}\epsilon_{zz}\Big]\,, \tag{B18}$$

where $\nu \approx 0.5$ refers to the Poisson ratio of the collagen cage. The total energy that is stored in stretching of the collagen cage is given by $F_s[u, u_\parallel] = \int dS_0\, f_s$, and is thus a functional of the surface deformation field $(u, u_\parallel)$. Here, $\int dS_0$ refers to a surface integral over the reference configuration of the collagen cage. In the cylindrical reference configuration, the (positive definite) stretching energy F_s vanishes and is therefore minimal. Consequently, any deformation of the collagen cage is accompanied by a finite energy cost so that a further deflection $(u, u_\parallel) \to (u + \delta u, u_\parallel + \delta u_\parallel)$ costs an energy $\delta F_s = F_s[u + \delta u, u_\parallel + \delta u_\parallel] - F_s[u, u_\parallel]$. When external stresses are relieved, the collagen cage will gradually move back from the deformed configuration to its reference configuration by releasing the stored elastic stretching energy in the form of work. Thus, stretching of the collagen cage induces elastic stresses that drive movement towards the mechanical reference configuration. We distinguish between two possible (and independent) directions of movement, axial/tangential and radial/normal, which couple to the respective stress fields. Tangential movement by some infinitesimal distance $\delta u_\parallel$ is driven by a *shear stress* along the interface:

$$\begin{aligned}\sigma_{cage}^{rz} = -\frac{\delta F_s}{\delta u_\parallel} &= -\frac{E_{cage}\, h}{2\,(1-\nu^2)}\,\frac{\delta}{\delta u_\parallel}\int dS_0\left[\Big(\frac{u}{R_0}\Big)^2 + \Big(\partial_z u_\parallel\Big)^2 + 2\nu\Big(\frac{u}{R_0}\Big)\Big(\partial_z u_\parallel\Big)\right] \\ &= \partial_z\left[\frac{E_{cage}\, h}{1-\nu^2}\Big(\epsilon_{zz} + \nu\epsilon_{\phi\phi}\Big)\right]\,.\end{aligned} \tag{B19}$$

Here, the term in square brackets corresponds to the axial component of the elastic surface tension in response to deformations of the thin shell. Specifically, by identifying the axial tension with $\tau_{el,zz} := \partial f_s/\partial\epsilon_{zz}$, cf. Eq. (B18), one finds that $\sigma_{cage}^{rz} = \partial_z \tau_{el,zz}$. Thus, Eq. (B19) illustrates that tangential shear stresses correspond to surface tension gradients, where regions with larger tension effectively pull on regions with lower tension.

These elastic shear stresses in the organoid branch are balanced by viscous stresses of the fluid that fills the organoid branch and by elastic stresses of the extracellular matrix. Since the cells are motile, they can move relative to the collagen cage. By extension of argument, the collagen cage can *slip* against the cell sheet and the fluid in the lumen of the organoid branch, so that the tangential shear stresses induced by the collagen cage relax quickly compared to the normal stresses. Assuming such a timescale separation, the tangential shear stresses in the collagen cage will vanish on the timescales relevant for perpendicular motion of the interface[9]. Then, one finds from Eq. (B19) that $\epsilon_{zz} = C - \nu\epsilon_{\phi\phi}$, where C is some constant. With this adiabatic approximation, the free energy density (per surface area) that is stored in stretching deformations of the tubular shell simplifies to:

$$f_s^\star = \frac{E_{cage}\, h}{2}\left[\epsilon_{\phi\phi}^2 + \frac{C^2}{(1-\nu^2)}\right] . \tag{B20}$$

Since, by definition, both the free energy that is stored in deformations and the corresponding tensions vanish in the reference configuration, the constant $C = 0$ must also vanish. Just as tangential movement is driven by a *shear stress* along the interface, perpendicular motion of the surface by some infinitesimal distance δu is driven by a *normal stress* that acts on the surface:

$$\Delta p_s = -\frac{\delta F_s}{\delta u} \approx \partial_u f_s^\star = -\frac{1}{R_0}\left[E_{cage}\, h\, \frac{u}{R_0}\right] . \tag{B21}$$

The deformed radius of the tubular shell is given by $R = R_0 + u$ and the reference radius is given by R_0. The term in square brackets corresponds to the circumferential component of the elastic surface tension in response to deformations of the thin shell. Thus, Eq. (B21) can be understood as a Laplace pressure that is associated with tension due to elastic deformations.

Passive bending of the collagen cage is counteracted by elastic stresses. Next, we discuss the Helfrich free energy density per surface area that is stored in bending deformations of the collagen cage [16]:

$$f_b = \frac{1}{2}k_b\left[(\kappa_\phi - c_\phi)^2 + (\kappa_z - c_z)^2\right] , \tag{B22}$$

where c_ϕ is the circumferential spontaneous curvature and c_z is the axial spontaneous curvature of the tubular shell. In the following, we assume that the tubular shape corresponds

---

[9] For a more general treatment, we would have to explicitly model the relaxation dynamics of the tangential shear stresses by considering the viscous properties of the collagen cage and/or the surrounding elastic medium.

to the mechanical reference configuration of the organoid branch, which therefore minimizes the bending energy. Thus, we set the axial spontaneous curvature to $c_z = 0$ and the circumferential spontaneous curvature to $c_\phi = -1/R_0$. This is a plausible ansatz since the collagen cage grows due to the contractility of the pre-existing organoid branch and persists even after washing out the epithelial cells [1]. Nevertheless, one would have to modify this assumption if the initial tubular shape corresponds to a pre-strained configuration, or if the shell-like organoid branch itself also significantly contributes to the bending energy[10]. For small deformations u, the two principal curvatures of the tubular shell are in good approximation given by $\kappa_z = \partial_z^2 u$ and $\kappa_\phi = -1/R$, along the axis z and the circumference ϕ respectively, cf. Eq. (B6). The free energy density (per surface area) that is stored in deformations of the collagen cage is then given by:

$$f_b = \frac{1}{2} k_b \left[\left(\frac{1}{R} - \frac{1}{R_0} \right)^2 + (\partial_z^2 u)^2 \right] \approx \frac{1}{2} k_b \left[\frac{u^2}{R_0^4} + (\partial_z^2 u)^2 \right] , \tag{B23}$$

for sufficiently small deformations of the tubular shell, $u \ll R_0$. The total bending energy of the collagen cage is given by $F_b[u] = \int dS_0 \, f_b$, and is a functional of the radial component of the surface deformation field, u. Here, as above, $\int dS_0$ refers to a surface integral over the reference configuration of the collagen cage. In the cylindrical reference configuration, the (positive definite) bending energy F_b vanishes and is therefore minimal. Consequently, any deformation of the collagen cage is accompanied by a finite energy cost so that a further deflection $u \to u + \delta u$ costs an energy $\delta F_b = F_b[u + \delta u] - F_b[u]$. When external stresses are relieved, the collagen cage will gradually move back from the deformed configuration to its reference configuration by releasing the stored elastic bending energy in the form of work. Thus, bending deformations of the collagen cage induce elastic stresses that drive movement towards the mechanical reference configuration. In principle, as above, we distinguish between two possible (and independent) directions of movement, axial/tangential and radial/normal, which couple to the respective stress fields. However, since the free energy that is stored in bending deformations does not depend on the axial component of the deformation field, $\delta F_b / \delta u_\parallel = 0$, the tangential shear stresses vanish. Note that there is a deeper reason as to why there are no tangential shear stresses in response to bending. For tangen-

---

[10] Cell contractility can effectively lead to a spontaneous curvature of thin cell sheets due to an asymmetric positioning of the cells' actomyosin cytoskeleton relative to the middle surface of the cell sheet [17]. If the spontaneous curvature is induced by cell contractility, then it can also be influenced by the local orientation of cells.

tial deformations, the material points of the thin shell only move along the surface, thus leaving its shape unchanged. Since the bending energy (B23) only depends on the shape of the thin shell, it follows that tangential deformations cannot induce bending stresses. This only leaves perpendicular motion of the surface by some infinitesimal distance δu, which is driven by a *normal stress* that acts on the surface:

$$\Delta p_b = -\frac{\delta F_b}{\delta u} = -k_b \left[\frac{u}{R_0^4} + \partial_z^4 u \right] , \tag{B24}$$

where the deformed radius of the tubular shell is given by $R = R_0 + u$ and the reference radius is given by R_0. Summing up the stresses that arise in response to stretching and bending of the collagen cage, Eq. (B21) and Eq. (B24),

$$\Delta p_{cage} = -E_{cage}\, h \,\frac{u}{R_0^2} - k_b \left[\frac{u}{R_0^4} + \partial_z^4 u \right] , \tag{B25}$$

yields the *normal* component of the total boundary stress due to elastic deformations. As our notation suggests, one can interpret the *normal* component of the boundary stresses as a pressure jump between the lumen of the organoid branch and the surrounding medium. This corresponds to an effective pushing stress (if positive) or pulling stress (if negative) on the interface from outside of the organoid branch.

Linear stability analysis. A cylindrical configuration of the thin tubular shell (i.e. the organoid branch) is stable whenever the combined effect of all elastic stresses and the active cellular tension *counteracts* any small shape perturbation. In this section, we use this argument to find conditions for which a cylindrical shape becomes linearly unstable. To that end, as we have done in the previous sections, we consider rotationally symmetric deformations of the tubular shell, $R = R_0 + u$, that are small compared to the equilibrium radius of the tube, $u \ll R_0$. At the organoid branch interface, there is a local balance between fluid stress, generalized Laplace pressure [Eq. (B14)] and the elastic stress induced by deformations of the collagen cage [Eq. (B25)]:

$$\begin{aligned} \sigma_{visc}^{rr} &= p_0 - \frac{\tau_\phi}{R} + \tau_z \partial_z^2 u - E_{cage}\, h\, \frac{u}{R_0^2} - k_b \left[\frac{u}{R_0^4} + \partial_z^4 u \right] \\ &\approx p_0 - \frac{\tau_\phi}{R_0} + \left[\frac{\tau_\phi}{R_0^2} - \frac{E_{cage}\, h}{R_0^2} - \frac{k_b}{R_0^4} + \tau_z \partial_z^2 - k_b \partial_z^4 \right] u \,. \end{aligned} \tag{B26}$$

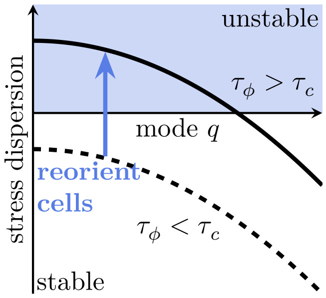

Supplementary Fig. 11. Stress dispersion relation as a function of the mode q. A reorientation of cells can increase the circumferential tension at the expense of the axial tension, thus shifting the stress dispersion relation upwards (blue arrow) and inducing a band of unstable modes.

The left-hand side of the stress-balance equation, Eq. (B26), corresponds to dynamic viscous stresses σ^{rr}_{visc} that vanish in steady state. Hence, only the right-hand side of the stress-balance equation (B26), where we have collected the hydrostatic pressure, the generalized Laplace pressure, and elastic stresses, determines the stability of the tubular shell. The stress-balance equation, Eq. (B26), must hold for any deformation of the tubular shell, including the reference configuration itself ($u = 0$). Therefore, the hydrostatic pressure is given by $p_0 = \tau_\phi / R_0$. Finally, we express the small deformations u in terms of Fourier components, $u = \sum_q u_q \cos(qz)$, and thus obtain the following stress dispersion relation near mechanical equilibrium [Fig. 11]:

$$\Delta p_q = \left[\frac{\tau_\phi}{R_0^2} - \frac{E_{cage}\, h}{R_0^2} - \frac{k_b}{R_0^4} - \tau_z q^2 - k_b q^4 \right] u_q \,. \tag{B27}$$

Since the last two terms of equation (B27) are stabilizing (positive axial tension τ_z and positive bending rigidity k_b), a band of unstable modes can only emerge if[11]:

$$\tau_\phi > \tau_c = E_{cage}\, h + \frac{k_b}{R_0^2} \,. \tag{B28}$$

These results indicate a long-wavelength instability according to the Cross/Hohenberg classification scheme [19]; specifically, the mechanical driving stress is largest for the $q = 0$ mode. However, note that here this will not be the fastest-growing mode, as homogeneous modes $q = 0$ are prohibited by the incompressibility of the fluid in the lumen of the organoid branch.

---

[11] The classical result for the pearling instability has an additional factor of $2/3$ in the second term, because it considers a material with zero spontaneous curvature along both principal directions [18]. Then, the bending energy acts as an additional destabilizing term.

In general, increasing the circumferential tension will increase the mechanical driving stress [cf. right-hand side of the stress-balance equation (B26)], and will therefore speed up the pearling instability. Furthermore, we note that the pearling instability occurs when the circumferential tension and the corresponding Laplace pressure are sufficiently strong to overcome the stabilizing effects conferred by the elastic properties of the collagen cage [Eq. (B27)]. As the alveolus grows, the Laplace pressure will then decrease, while the hydrostatic pressure will remain approximately constant (if the alveolus is still connected to an organoid branch). Furthermore, the stress due to elastic bending of the collagen cage is much smaller than the stress due to elastic stretching, given that the former scales with the thickness of the collagen cage h and the latter scales with h^3. Therefore, for a spherical alveolus whose radius grows from R_0 to R at the tip of an organoid branch, we can make the following approximation:

$$\sigma^{rr}_{visc} = \Delta p = \frac{\tau_\phi}{R_0} - \frac{\tau_\phi}{R} - E_{cage}\, h\, \frac{R - R_0}{R_0^2}\,. \tag{B29}$$

The final equilibrium radius of the alveolus is then determined by the steady-state condition $\sigma^{rr}_{visc} = 0$ and is therefore given by

$$\frac{R}{R_0} = \frac{\tau_\phi}{E_{cage}\, h}\,. \tag{B30}$$

We conclude that the above theory predicts that an increase in surface tension will lead to larger alveoli that also form faster. These results hold on sufficiently short timescales, where the deformation of the extracellular matrix is elastic and fully reversible. On long timescales, if the stresses in the extracellular matrix are above the plastic yield threshold, then the reference radius R_0 will effectively increase due to plastic deformation of the extracellular matrix thus leading to a robust and continued growth of spherical alveoli as we have discussed in the main text.

Estimating the critical circumferential tension. We next estimate the magnitude of the critical tension. For a homogeneously elastic sheet with elastic modulus E_{cage}, Poisson ratio ν and thickness h, the bending modulus is given by [5] $k_b = E_{cage}\, h^3/[12(1 - \nu^2)]$. In section A 3 "Collagen "cage"", confocal microscopy data showed that the collagen cage has a typical thickness of $h \simeq 5\,\mu\text{m}$. Furthermore, we have estimated in section A 3 "Collagen "cage"" that the elastic modulus of the collagen cage should lie in the range between $E_{cage} = 0.72\,\mathrm{kPa}$ and $E_{cage} = 1.38\,\mathrm{kPa}$. Furthermore, analogously to section A 3 "Collagen "cage"", we assume that the collagen cage (which has a collagen concentration of roughly $6.5\,\mathrm{mg\,ml^{-1}}$) is incompressible, such that $\nu = 1/2$ [20]. For a branch radius of $R_0 = 30\,\mu\mathrm{m}$, we find that the critical circumferential tension τ_c of the organoid branch [Eq. (B28)] lies in the range between $\tau_c = 3.6\,\mathrm{mN\,m^{-1}}$ and $\tau_c = 6.9\,\mathrm{mN\,m^{-1}}$. Values for the cortical tension of single contractile cells have been measured via micropipette aspiration to be about $0.4\,\mathrm{mN\,m^{-1}}$ for L929 fibroblasts [21] and have similar values for chick fibroblasts [22], $4.1\,\mathrm{mN\,m^{-1}}$ for Dictyostelium discoideum [23], and via traction force microscopy to reach up to $5\,\mathrm{mN\,m^{-1}}$ for human microvascular endothelial cells [24] (HMEC-1). Furthermore, micropipette aspiration of spheroids consisting of MCF-10A (human mammary epithelial) cells has yielded a value of $10\,\mathrm{mN\,m^{-1}}$ [25] for the corresponding surface tension.

We conclude that the active tension induced by cellular contractility is strong enough to trigger a pearling instability against the mechanical resistance of the collagen cage. In addition, the active tension induced by cellular contractility is sufficiently small so that an axial alignment of cells [cf. section B 2 "Active cell contractility induces anisotropic tension and Laplace pressure"] could keep the circumferential component of the tension tensor below the critical value, Eq. (B28). Finally, our cell tracking data show that collective rotations of cells around the circumference of the organoid branch typically begin at the tips of the organoid branches [cf. Fig. 3 in the main text]. This observation is rooted in the fact that at the tips of the organoid branches, cells have to repolarize and either migrate back or begin collectively migrating around the circumference (i.e. rotations); the latter corresponds to the least frustrated state where cells can keep migrating with the least number of changes in direction. Therefore, cell reorientation and an increase in circumferential tension at the expense of axial tension also typically begin at the tips of the organoid branches. Furthermore, note that Buchmann and Meixner et al. [1] have shown that the collagen cage is thinner at the organoid branch tips and approaches a thickness of up to $h = 10\,\mu\mathrm{m}$ towards the organoid body. In that case, the critical tension would increase by a factor of at least 2 (relative to our estimated value, assuming that the collagen cage has the same elastic modulus near the organoid body) towards the organoid body. These two observations (preferred cell reorientation and thinner collagen cage) rationalize why the pearling instability preferably occurs at the organoid branch tips.

4. Bulk extracellular matrix elasticity does not significantly affect tube stability

So far, we have assumed that a tubular configuration of the shell-like organoid branch is stabilized by a rigid collagen cage. In addition, the organoid branch is also surrounded by an elastic extracellular matrix. Thus, one may wonder whether a collagen cage is required, or if a homogeneous extracellular matrix itself would be sufficient to stabilize tubular shapes. In the following, we argue that a homogeneously elastic extracellular matrix is too soft to stabilize the cylindrical organoid branch against its own contractility.

To that end, we use linear elasticity theory. The extracellular collagen matrix is a three-dimensional body and thus requires a treatment in terms of three-dimensional bulk coordinates

$$\mathbf{r}(r, z, \phi) = \begin{bmatrix} r\cos\phi \\ r\sin\phi \\ z \end{bmatrix} , \tag{B31}$$

which match the surface coordinates at the interface of our tubular geometry [cf. section B 1 "Choice of coordinate system"]. The three (orthogonal but non-normalized) basis vectors that span the three-dimensional of our tubular geometry are then given by

$$\mathbf{b}_r = \begin{bmatrix} \cos\phi \\ \sin\phi \\ 0 \end{bmatrix} , \quad \mathbf{b}_z = \begin{bmatrix} 0 \\ 0 \\ 1 \end{bmatrix} , \quad \text{and} \quad \mathbf{b}_\phi = \begin{bmatrix} -r\sin\phi \\ r\cos\phi \\ 0 \end{bmatrix} . \tag{B32}$$

In the present section, we use contravariant notation to express vectors, $\mathbf{v} = v^i\,\mathbf{b}_i$, and tensors, $\boldsymbol{\sigma} = \sigma^{ij}\,\mathbf{b}_i \otimes \mathbf{b}_j$. Contravariant notation indicates that the components of any vector field, v^i, transform inversely in response to any basis transformation, so that the vector field $\mathbf{v}$ itself remains invariant. As before, we assume a rotational symmetry around the z-axis.

We associate the mechanical reference configuration of the organoid branch and of the extracellular matrix with the initial shape of the tubular shell. Then, we consider infinitesimal deviations from this reference configuration, which are parameterized by the deformation field $\mathbf{u}$. The corresponding linearized strain tensor is given by [5]:

$$\boldsymbol{\epsilon}_{lin} = \frac{1}{2}\left[\boldsymbol{\nabla}\otimes\mathbf{u} + (\boldsymbol{\nabla}\otimes\mathbf{u})^T\right] = \sum_{i,j\in\{r,\phi,z\}} \epsilon^{ij}\,\mathbf{b}_i\otimes\mathbf{b}_j\,. \tag{B33}$$

In contrast to section A 3 “Collagen “cage””, as discussed above, we have here expressed the linearized strain tensor in contravariant notation. In our rotationally symmetric cylindrical coordinate system, the strain tensor is given by:

$$\boldsymbol{\epsilon}_{lin} \equiv \begin{bmatrix} \epsilon^{rr} & \epsilon^{rz} & \epsilon^{r\phi} \\ \epsilon^{zr} & \epsilon^{zz} & \epsilon^{z\phi} \\ \epsilon^{\phi r} & \epsilon^{\phi z} & \epsilon^{\phi\phi} \end{bmatrix} = \begin{bmatrix} \partial_r u^r & (\partial_z u^r + \partial_r u^z)/2 & \partial_r u^\phi/2 \\ (\partial_z u^r + \partial_r u^z)/2 & \partial_z u^z & \partial_z u^\phi/2 \\ \partial_r u^\phi/2 & \partial_z u^\phi/2 & u^r/r^3 \end{bmatrix}. \tag{B34}$$

The trace of the strain tensor in our cylindrical coordinate system,

$$\begin{aligned} \mathrm{tr}_g(\boldsymbol{\epsilon}_{lin}) &= \sum_{i\in\{r,\phi,z\}} \hat{\mathbf{b}}_i\cdot\boldsymbol{\epsilon}_{lin}\cdot\hat{\mathbf{b}}_i = \epsilon^{rr} + \epsilon^{zz} + r^2\epsilon^{\phi\phi} \\ &= \partial_z u^z + \frac{1}{r}\partial_r(r\,u^r) = \boldsymbol{\nabla}\cdot\mathbf{u}\,, \end{aligned} \tag{B35}$$

indicates volumetric changes (i.e. isotropic compression and dilatation) due to the deformation field u. Splitting the strain tensor into a pure shear component and a pure volumetric part, the linear elastic stress tensor is given by [5]:

$$\begin{aligned} \boldsymbol{\sigma}_{el} &= 2\mu\left[\boldsymbol{\epsilon}_{lin} - \frac{1}{3}\,\mathrm{tr}_g(\boldsymbol{\epsilon}_{lin})I_3\right] + \frac{2\mu}{3}\frac{1+\nu}{1-2\nu}\,\mathrm{tr}_g(\boldsymbol{\epsilon}_{lin})I_3 \\ &= 2\mu\left[\boldsymbol{\epsilon}_{lin} + \frac{\nu}{1-2\nu}\,\mathrm{tr}_g(\boldsymbol{\epsilon}_{lin})I_3\right]\,, \end{aligned} \tag{B36}$$

where I_3 refers to the identity matrix. A mechanical force balance in the bulk of the extracellular matrix implies that the body force that acts on an infinitesimal volume element vanishes [26]:

$$\mathbf{f} = \boldsymbol{\nabla}\cdot\boldsymbol{\sigma}_{lin} = \begin{bmatrix} \frac{1}{r}\partial_r(r\sigma_{el}^{rr}) + \partial_z\sigma_{el}^{rz} - r\sigma_{el}^{\phi\phi} \\ \frac{1}{r}\partial_r(r\sigma_{el}^{rz}) + \partial_z\sigma_{el}^{zz} \\ \frac{1}{r}\partial_r(r\sigma_{el}^{r\phi}) + \frac{2}{r}\sigma_{el}^{r\phi} + \partial_z\sigma_{el}^{z\phi} \end{bmatrix} = 0\,. \tag{B37}$$

The circumferential component of the body force vanishes in the absence of torques. Then, the remaining mechanical force balance equations in the bulk of the extracellular matrix are given by:

$$\partial_z\left[\frac{1}{1-2\nu}\frac{1}{r}\partial_r(r\,u^r)+2\frac{1-\nu}{1-2\nu}\partial_z u^z\right]+\frac{1}{r}\partial_r(r\,\partial_r u^z)=0, \tag{B38a}$$

$$\partial_r\left[2\frac{1-\nu}{1-2\nu}\frac{1}{r}\partial_r(r\,u^r)+\frac{1}{1-2\nu}\partial_z u^z\right]+\partial_z^2 u^r=0, \tag{B38b}$$

where u^r and u^z refer to the radial and axial deformation field, in contravariant notation, respectively. To solve these equations, we introduce the stress function Φ via an implicit definition:

$$u^r=-\partial_r\partial_z\Phi\,,\quad u^z=2(1-\nu)\Delta\Phi-\partial_z^2\Phi\,. \tag{B39}$$

By inserting Eq. (B39) into Eqs. (B38a) and (B38b), one finds that the stress function Φ must satisfy the biharmonic equation in cylindrical coordinates [26]:

$$\Delta^2\Phi=0\,. \tag{B40}$$

We are interested in undulations of the tubular organoid branch, and therefore decompose the deformation field of the extracellular matrix into Fourier modes: $u^r=\sum_q u_q^r(r)\cos(qz)$ and $u^z=\sum_q u_q^z(r)\sin(qz)$. Thus, we may also express the stress function in terms of Fourier modes: $\Phi=\sum_q\Phi_q(r)\sin(qz)$. The general real-valued solution to the biharmonic equation (B40) is then given by:

$$\Phi_q(r)=a_1\Big[Y_0(-iqr)+iI_0(qr)\Big]+a_2I_0(qr)+ia_3r\Big[I_1(qr)+Y_1(-iqr)\Big]+a_4rI_1(qr)\,, \tag{B41}$$

where $I_k(x)$ refers to the modified Bessel function of the first kind and $Y_k(x)$ refers to the Bessel function of the second kind, respectively. As we consider the extracellular matrix as an elastic medium in the half-space $r\geq R$, we are only interested in real-valued solutions (u^r,u^z) that decay in the far field and approach zero as $r\to\infty$. This constraint fixes two of the four coefficients in Eq. (B41), $a_2=0$ and $a_4=0$, which correspond to solutions that would vanish at $r\to 0$ and diverge in the far field $r\to\infty$. The remaining two coefficients a_1 and a_3 can be determined by imposing boundary conditions on the deformation field. Here, we choose a general radial deformation, $u_q^r(R)$, and impose no-slip conditions on the axial

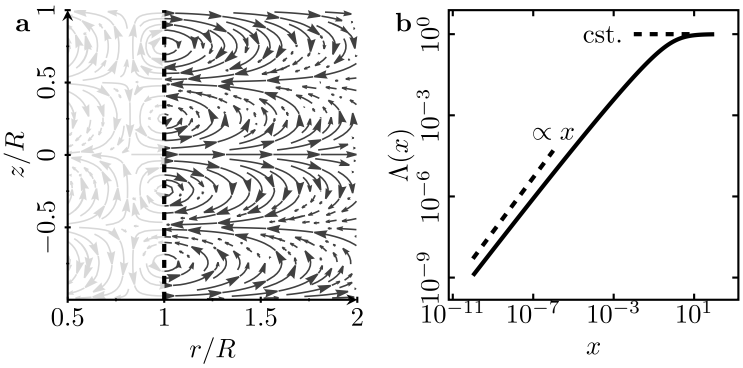

Supplementary Fig. 12. **a)** Exemplary deformation field around a tubular branch, for an incompressible extracellular matrix $\nu = 1/2$ and a Fourier mode $q = 2\pi/R$. The gray region indicates the wall of the organoid branch. **b)** Illustration of the function $\Lambda(x)$, which saturates (dashed line) for large arguments and grows (approximately) linearly for small arguments. Thus, the normal component of the elastic stress grows quadratically for small arguments qR and linearly for large arguments qR. For simplicity, we have assumed an incompressible material, $\nu = 1/2$.

deformation, $u_q^z(R) = 0$. Then, the stress function is given by the following expression:

$$\Phi_q(r) = \frac{u_q^r(R)}{q^2} \frac{K_0(qr)}{K_1(qR)} \left[1 + q\,\Theta(qR) \left(RB(qR) - \frac{r}{B(qr)} \right) \right] , \tag{B42}$$

where we have defined

$$\Theta(x) := \frac{B(x)}{x - B(x)\big[4(1-\nu) + xB(x)\big]} , \quad \text{and} \quad B(x) := \frac{K_0(x)}{K_1(x)} , \tag{B43}$$

and where $K_k(x)$ refers to the modified Bessel function of the second kind. Using Eq. (B39), we readily obtain the full (rotationally symmetric) deformation field of the extracellular matrix. Then, we calculate the radial component of the elastic stress tensor, σ_{el}^{rr}, where μ refers to the shear modulus of the extracellular matrix [cf. Eq. (B36)]:

$$\sigma_{el}^{rr}(R) = -\frac{2\mu}{R} \sum_q \Big(1 + qR\Lambda(qR) \Big)\, u_q^r(R)\, \cos(qz) , \tag{B44a}$$

$$\Lambda(x) := -2(1-\nu) B(x) \Theta(x) . \tag{B44b}$$

The above function $\Lambda(x)$ and the deformation field are depicted in Supplementary Fig. 12. For the no-slip boundary conditions that we have chosen here, the normal stress grows quadratically for small arguments $qR \ll 1$ and linearly for large arguments $qR \gg 1$.

Replacing the thin bendable collagen cage with an extended homogeneous extracellular matrix, the mechanical driving stress [cf. right-hand side of the stress-balance equation (B26)] on the shell-like organoid branch is given by

$$\Delta p_q = \left[\frac{\tau_\phi}{R_0^2} - \tau_z q^2 - \frac{2\mu}{R_0}\Big(1 + qR_0\,\Lambda(qR_0)\Big) \right] u_q\,. \tag{B45}$$

The first term (Laplace pressure due to circumferential tension) in the square brackets is destabilizing and does not depend on the wavelength. The second term (Laplace pressure due to axial tension) in the square brackets stabilizes short wavelengths. The third term in the square brackets (elastic stress) has a contribution that stabilizes long wavelengths ($q = 0$) and a contribution that stabilizes short wavelengths ($q > 0$). In particular, for the no-slip boundary conditions that we have chosen here, the function $\Lambda(x)$ grows monotonically as its argument x increases, cf. Supplementary Fig. 12b, with $x\Lambda(x) \propto x^2$ for small arguments. We conclude that a pearling-like instability at low wavelengths (i.e. for $q \to 0$) will only occur if the Laplace pressure due to circumferential tension can overcome the stabilizing effects conferred by the extracellular matrix:

$$\tau_\phi > 2\mu R_0 \tag{B46}$$

For a shear modulus of $\mu \approx 7\,\mathrm{Pa}$ this yields a critical surface tension of $0.4\,\mathrm{mN\,m^{-1}}$, which is far below the reference tension of $10\,\mathrm{mN\,m^{-1}}$ for the surface tension of spheroids consisting of MCF-10A (human mammary epithelial) cells [25]. Thus, we conclude that the homogeneous extracellular matrix alone is unlikely to stabilize a tubular geometry in our experiments, which further emphasizes the mechanical role of the collagen cage.

---

[1] Buchmann, B. *et al.* Mechanical plasticity of the ECM directs invasive branching morphogenesis in human mammary gland organoids. *To appear in Nat. Comm.* (2021). https://www.biorxiv.org/content/early/2019/11/29/860015.full.pdf.

[2] Schliwa, M. Action of cytochalasin D on cytoskeletal networks. *Journal of Cell Biology* **92**, 79–91 (1982).

[3] Berg, S. *et al.* ilastik: interactive machine learning for (bio)image analysis. *Nature Methods*

(2019).

[4] Brodland, G. W. *et al.* CellFIT: A cellular force-inference toolkit using curvilinear cell boundaries. *PLOS ONE* **9**, 1–15 (2014).

[5] Landau, L. *et al.* *Theory of Elasticity: Volume 7*. Course of theoretical physics (Elsevier Science, 1986).

[6] Kong, W. *et al.* Experimental validation of force inference in epithelia from cell to tissue scale. *Scientific Reports* **9**, 14647 (2019).

[7] Grinfeld, P. *Introduction to Tensor Analysis and the Calculus of Moving Surfaces* (Springer, 2013).

[8] Bischofs, I. B. & Schwarz, U. S. Cell organization in soft media due to active mechanosensing. *Proceedings of the National Academy of Sciences* **100**, 9274–9279 (2003). URL `https://www.pnas.org/content/100/16/9274`. https://www.pnas.org/content/100/16/9274.full.pdf.

[9] Bischofs, I. B., Safran, S. A. & Schwarz, U. S. Elastic interactions of active cells with soft materials. *Phys. Rev. E* **69**, 021911 (2004). URL `https://link.aps.org/doi/10.1103/PhysRevE.69.021911`.

[10] Safran, S. *Statistical Thermodynamics Of Surfaces, Interfaces, And Membranes* (CRC Press, Boca Raton, 2003).

[11] Raub, C., Putnam, A., Tromberg, B. & George, S. Predicting bulk mechanical properties of cellularized collagen gels using multiphoton microscopy. *Acta Biomaterialia* **6**, 4657 – 4665 (2010).

[12] Jansen, K. A. *et al.* The role of network architecture in collagen mechanics. *Biophysical Journal* **114**, 2665–2678 (2018).

[13] Liu, B., Zhang, L. & Gao, H. Poisson ratio can play a crucial role in mechanical properties of biocomposites. *Mechanics of Materials* **38**, 1128 – 1142 (2006).

[14] Timoshenko, S. P. & Gere, J. M. *Theory of Elastic Stability* (Dover Publications, 1961).

[15] Hannezo, E., Prost, J. & Joanny, J.-F. Mechanical instabilities of biological tubes. *Physical Review Letters* **109**, 018101 (2012). URL `https://doi.org/10.1103/PhysRevLett.109.018101`.

[16] Helfrich, W. Elastic properties of lipid bilayers: Theory and possible experiments. *Zeitschrift für Naturforschung C* **28**, 693–703 (1973). URL `https://doi.org/10.1515/znc-1973-11-1209`.

[17] Hannezo, E., Prost, J. & Joanny, J.-F. Theory of epithelial sheet morphology in three dimensions. *Proceedings of the National Academy of Sciences* **111**, 27–32 (2014).

[18] Bar-Ziv, R. & Moses, E. Instability and "pearling" states produced in tubular membranes by competition of curvature and tension. *Phys. Rev. Lett.* **73**, 1392–1395 (1994). URL `https://link.aps.org/doi/10.1103/PhysRevLett.73.1392`.

[19] Cross, M. C. & Hohenberg, P. C. Pattern formation outside of equilibrium. *Rev. Mod. Phys.* **65**, 851–1112 (1993). URL `https://link.aps.org/doi/10.1103/RevModPhys.65.851`.

[20] Castro, A. P. G. *et al.* Combined numerical and experimental biomechanical characterization of soft collagen hydrogel substrate. *J. Mater. Sci. Mater. Med.* **27**, 79 (2016).

[21] Tinevez, J.-Y. *et al.* Role of cortical tension in bleb growth. *Proceedings of the National Academy of Sciences* **106**, 18581–18586 (2009).

[22] Thoumine, O., Cardoso, O. & Meister, J.-J. Changes in the mechanical properties of fibroblasts during spreading: a micromanipulation study. *European Biophysics Journal* **28**, 222–234 (1999). URL `https://doi.org/10.1007/s002490050203`.

[23] Winklbauer, R. Cell adhesion strength from cortical tension - an integration of concepts. *J. Cell Sci.* **128**, 3687–3693 (2015).

[24] Bastounis, E. E., Ortega, F. E., Serrano, R. & Theriot, J. A. A multi-well format polyacrylamide-based assay for studying the effect of extracellular matrix stiffness on the bacterial infection of adherent cells. *JoVE* e57361 (2018). URL `https://www.jove.com/t/57361`.

[25] Villeneuve, C. *et al.* aPKCi triggers basal extrusion of luminal mammary epithelial cells by tuning contractility and vinculin localization at cell junctions. *Proceedings of the National Academy of Sciences of the United States of America* **116**, 24108–24114 (2019). URL `https://doi.org/10.1073/pnas.1906779116`.

[26] Amenzade, I. *Theory of Elasticity* (Mir, 1979).